Nanoscale

PAPER

View Article Online
View Journal | View Issue

Cite this: *Nanoscale*, 2023, **15**, 6976

GeSe-evoked synchronous strategy for electrodeposited CZGSe solar cells†

Jingling Liu,‡ Kang Gao,‡ Hang Cai, Xinyu Wu, Xinsheng Liu, Ke Cheng* and Zuliang Du *

Received 29th December 2022,
Accepted 3rd March 2023

DOI: 10.1039/d2nr07285h

rsc.li/nanoscale

Sn-free $Cu_2ZnGeSe_4$ (CZGSe) is emerging as a promising non-toxic and earth-abundant photovoltaic absorber material due to its attractive electrical and optical properties as well as its high theoretical conversion efficiency. Nevertheless, no photovoltaic device fabricated through the green electrodeposition process has yet been reported, likely due to the poor solubility of Ge-based salts and harsh electrodeposition conditions. Herein, we propose a GeSe-evoked synchronous strategy involving a Ge incorporation and selenization-regulated co-heating process of GeSe and Se, following electrodeposition of a Cu–Zn preformed layer. We experimentally found that the low-melting-point GeSe could promote the crystal growth and induce a high-quality bulk absorber layer and good back interface. In the GeSe-promoted sample, it was found that $MoSe_2$ could ensure a good back quasi-Ohmic contact, and the band bending at the grain boundaries (GBs) was favorably inverted. Moreover, the depletion region width was also prolonged, and the deleterious Cu_{Zn} near E_F was passivated, leading to an increased carrier separation. In turn, a surprising progress in device performance was found, achieving a ground-breaking efficiency of 3.69%, and it could fill the bank of green electrodeposited CZGSe-based solar cells.

1. Introduction

$Cu_2ZnSn(S,Se)_4$ (CZTSSe) kesterite-based thin-film solar cells have attracted extensive attention because of their green earth-abundant elements, suitable direct bandgaps, strong optical absorption coefficient, and high theoretical conversion efficiency.[1,2] However, in CZTSSe absorbers, the key parameter that limits their high efficiency is their low open-circuit voltage (V_{OC}), which drags down their efficiency, peaking at only 13% thus far.[3–6] Compositional inhomogeneities, Cu/Zn disorders, and interface recombination are considered to be the key factors for the voltage loss.[5–8] Besides, the multivalence Sn element, which can exist in many adverse forms, such as Sn–Se secondary phases, has been identified as one of the main detrimental issues.[9,10]

To overcome the Sn-associated issues, the substitution of Ge for Sn has shown enormous beneficial effects on kesterite-based devices, including favoring the crystallinity growth, reducing Sn-related defects, and improving the carrier lifetime.[9–11] Inspired by this, Sn-free $Cu_2ZnGeSe_4$ (CZGSe) absorbers have begun to attract significant interest recently based on the following favorable aspects: (1) CZGSe has a higher Shockley–Queisser (SQ) limit of 33.3% due to its optimal band gap. Its trap-limited conversion (TLC) efficiency of 24.1% is also higher than that of $Cu_2ZnSnSe_4$ (CZTSe, 20.3%) and Cu_2ZnSnS_4 (CZTS, 20.9%);[12] (2) Cu_{Zn} defects are suppressed in CZGSe as compared to in Sn-based kesterite, as Ge_{Zn}-induced recombination is lower than that of Sn_{Zn} due to its deeper donor level;[12–14] (3) the sub-band-gap absorption induced by disorders is less, because of the larger formation energies of stannite and kesterite phases (64 meV for CZGSe, 42 meV for CZTSe), leading to a low E_u value.[12,13] A highest V_{oc} of 744 mV in CZGSe-based solar cells was reported by Sahayaraj *et al.* with a PCE of 5.5%.[15] A record efficiency of 8.5% was achieved through interface engineering.[16]

Despite its advantages over Sn-based kesterite solar cells, its efficiency remains low. This is mainly ascribed to defect complexation (Cu_{Zn}–Ge_{Zn} *etc.*) rooted in the similar redox activity of Ge to Sn, leading to a high nonradiative recombination in CZGSe.[12,13,17] Besides, the band alignment between CZGSe and CdS is a cliff-type, which works against it in photovoltaic applications.[16,18] Therefore, more efforts are required to fully understand and optimize this material. The phase impurities often serve as recombination centers, causing serious carrier recombination, and are thus detrimental to device efficiency.

Key Laboratory for Special Functional Materials of Ministry of Education, National & Local Joint Engineering Research Center for High-efficiency Display and Lighting Technology, School of Materials Science and Engineering, and Collaborative Innovation Center of Nano Functional Materials and Applications, Henan University, Kaifeng 475004, China. E-mail: zld@henu.edu.cn, ck@henu.edu.cn

†Electronic supplementary information (ESI) available. See DOI: https://doi.org/10.1039/d2nr07285h

‡These authors contributed equally to the work.

Several strategies have been produced to address this, such as vacuum-based magnetron sputtering/electron beam evaporation and organic solvents-based solution process.[15,19–24] However, these strategies generally involve high costs, less security, and/or intricate deposition technologies. Thus, to explore low-cost, green, and simple new synthesis technology, optimizing the appropriate absorber conditions and purifying the phase impurities are the most important priorities at present.

In this work, high-quality CZGSe thin films were achieved through a simple combination of the green electrodeposition and selenization processes. In view of the poor solubility of Ge-based salts and harsh electrodeposition requirements, GeSe with a low melting point and high saturated vapor pressure at evaluated temperature was selected as the Ge source. A synchronous strategy of Ge incorporation and selenization was well designed through a co-heating process of GeSe and Se following the electrodeposition of a Cu–Zn preformed layer. Furthermore, the advantages of GeSe over $GeSe_2$ for the film quality and device performance were addressed in detail.

2. Experimental

2.1. Preparation of Cu–Zn preformed layers

A Cu–Zn preformed layer was first electrodeposited on Mo-coated SLG substrates (2×2 cm^2), similar to in our previous reports.[25,26] Briefly, $CuSO_4$ and $ZnSO_4$ were employed as Cu and Zn sources, and sodium citrate was used as the complexing agent. A potentiostatic mode was applied using a three-electrode system, where Ag/AgCl and Pt net served as the reference and counter electrodes, respectively. Cu and Zn metal layers were successively electrodeposited with constant potentials of −0.35 and −1.15 V, respectively. After this, the samples were washed with DI water and dried with N_2 gas.

2.2. Preparation of CZGSe absorber layers

According to the different characteristics of the Ge sources, two schemes for the preparation of CZGSe absorber layers were proposed: (1) a two-step process, whereby the Cu–Zn prefabricated layer was first placed in a round graphite box containing 100 mg $GeSe_2$ powder and kept at 600 °C for 30 min for Ge incorporation. Subsequently, the samples were selenized through a two-step RTP annealing system in 100 mg Se and a tiny amount of $GeSe_2$ (5 mg) in an Ar flow to make them well-crystallized. To optimize the CZGSe thin films, different selenization temperatures (480 °C, 500 °C, 520 °C) were used; (2) a one-step process, whereby Ge incorporation and selenization was realized through co-heating mixed GeSe and Se powder in an RTP annealing system. Se powder (100 g) and 100 mg of GeSe were placed in a graphite box and annealed at 280 °C and 600 °C for 30 min in an Ar atmosphere and then allowed to cool to room temperature naturally. Similarly, different selenization temperatures (580 °C, 600 °C, 620 °C) were applied to obtain the optimized films. The heating rate for all the steps was set at 7 °C s^{-1}. The samples prepared by the two-step process and one-step process were defined as CZGSe-A and CZGSe-B, respectively. The specific procedures are sketched out in Fig. 1.

2.3. CZGSe solar cells fabrication

CZGSe solar cells were fabricated with a structure of SLG/CZGSe/CdS/i-ZnO/ITO/Ag. First, 60 nm of CdS as a buffer layer was deposited on the CZGSe thin films by chemical bath deposition (CBD). In quick succession, the intrinsic-ZnO (i-ZnO, 50 nm) and indium tin oxide ($SnO_2:In_2O_3$, ITO, 250 nm) window layers were deposited by radiofrequency (RF) sputtering. The marked Ag as the top contact was evaporated. Finally, an individual solar cell with an active area of 0.21 cm^2 was defined by mechanical scribing. Neither surface treatments nor an anti-reflective coating were used.

2.4. Characterization

Scanning electron microscopy (SEM) images were obtained with a Nova NanoSEM 450 system, equipped with an energy dispersive X-ray spectroscopy (EDX) unit. The powder X-ray diffraction (XRD, MRD-Philips) patterns were collected with a Bruker D8-diffractometer using monochromatized Cu Kα radiation. A model TGA 6000 instrument was applied for the thermogravimetric analysis (TGA). Raman spectra (Renishaw inVia) were recorded with the wavelength excitation of 785 nm. X-Ray photoelectron spectroscopy (XPS) was performed using an Al Kα source (ESCALAB 250). The photocurrent density–voltage (J–V) curves were obtained using a Newport optical power meter (model 842-PE) with a Keithley 2400 source meter. The light intensity was 100 mW cm^{-2} as certified by a Si reference cell. The external quantum efficiency (EQE) spectra were obtained on a Zolix SCS100 QE system. Kelvin probe force microscopy (KPFM) was performed to obtain the surface potentials. Capacitance–voltage (C–V) curves were determined with a bias range of −1 to +1 V using a Keithley 4200A-SCS system with 10 kHz frequency at room temperature. Capacitance-mode deep-level transient spectroscopy (C-DLTS) was conducted in the range from 120 K to 240 K. Admittance scans were taken using a Keithley 4200A-SCS system in a frequency range of 10^3 to 10^7 Hz with a 30 mV alternating current (AC) amplitude and 0 V direct current (DC) bias in the dark. Electrochemical impedance spectroscopy (EIS) measurements were collected in the frequency range of 10^2–10^6 Hz without bias, under AM 1.5 G sun illumination.

3. Results and discussion

To electrodeposit Ge thin films in aqueous or nonaqueous electrolytes is extremely difficult, because of the poor solubility of Ge-based salts and/or harsh electrodeposition conditions.[27,28] Therefore, it is inadvisable to obtain Ge films through the electrodeposition process. Furthermore, Ge is generally introduced by thermal evaporation, magnetron sputtering, or an organic solvent-based solution process, but with high-standard equipment and under rigorous conditions.[21–24] Thus, new synthetic technology for Ge incorporation into an

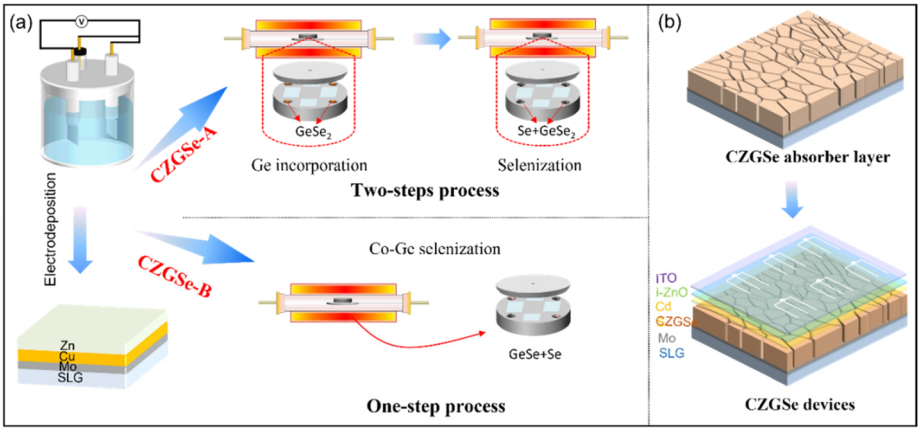

Fig. 1 (a) Schematic diagram of CZGSe absorbers prepared by a two-step and one-step process, involving electrochemical deposition and selenization. (b) As-prepared CZGSe absorber layer and its corresponding solar cell device.

electrodeposited prefabricated layer, which possesses the capacity for low-demanding equipment and high safety factors was proposed in this work.

Two schemes are proposed according to the different characteristics of Ge sources and that include solution preparation, electrodepositing a Cu/Zn prefabricated layer, Ge incorporation, and selenization, as illustrated in Fig. 1. The following grounds are considered for these procedures: (1) Ge is quite inappropriate due to its high melting point over 900 °C; (2) to avoid the introduction of heteroatoms, only selenides, such as $GeSe_2$ and GeSe, are the right candidates; (3) experimentally, it was found that Ge is seriously insufficient obtained through a one-step co-heating of $GeSe_2$ and Se. Therefore, two steps were involved for the $GeSe_2$-based process; (4) taking into account the low melting point and easy sublimation properties as discussed below, GeSe is, undoubtedly, the most suitable candidate.[29,30]

To guide the experimental design, the thermodynamic properties were first investigated as shown in Fig. 2a and b. Under certain conditions, the vapor pressure determines the evaporation difficulty and relative contents of the corresponding products, deeply impacting the film quality. Thus, the temperature-dependent vapor pressures for GeSe, $GeSe_2$, Ge, and Se were calculated according to the equation: $\log p = A - B/T$, where p is the vapor pressure, A and B are constants and their specific values are given in the literature,[29] and T is the absolute temperature. As shown in Fig. 2a, GeSe had a higher vapor pressure than that of $GeSe_2$, second only to Se. Importantly, the vapor pressure of GeSe rapidly increased at 450 °C, below its melting point of 670 °C. Although the melting points of $GeSe_2$ (700 °C) and GeSe were similar, their vapor pressures at elevated temperatures were far different, indicating GeSe evaporated more easily than $GeSe_2$. Ge had almost no vapor below 600 °C, thus directly ruling it out. To experimentally confirm the calculated results, TGA was performed and the results are provided in Fig. 2b. GeSe showed weight loss with a starting point near 500 °C, below its melting point, while $GeSe_2$ had a much higher starting point near 600 °C, consistent with the

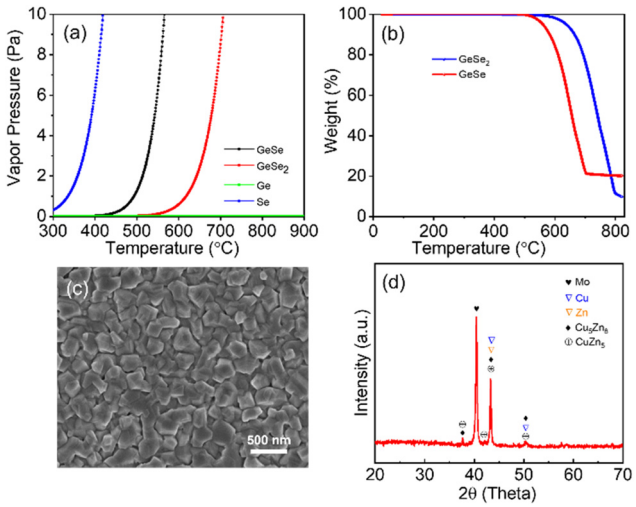

Fig. 2 (a) Temperature-dependent vapor pressures of $GeSe_2$, GeSe, Ge, and Se powders. (b) TGA plots of $GeSe_2$ and GeSe powders. (c and d) SEM image and XRD patterns of the electrodeposited Cu–Zn preformed layer.

above calculations. Moreover, a lower evaporation temperature was also needed for our RTP experiment design. Taking this as a guide, the setting temperature should be close to or slightly above the evaporation temperature to ensure sufficient Ge vapor species.

Before the preparation of CZGSe thin films, the Cu/Zn preformed layer was first electrodeposited onto Mo-coated SLG as provided in Fig. 2 and S1.† Fig. 2c shows that the Cu/Zn preformed layer had a dense crystalline morphology, consistent with that of electrodeposited CZTSe in our previous work.[25,26] From XRD, Cu–Zn alloys were observed, probably combined with Cu and Zn metal phases. Fig. S1† shows the EDX line scans, presenting clear Cu and Zn lines with a partial overlap, which could be assigned to Cu–Zn alloys.

The typical morphology and structure characterization of the absorber layers prepared with $GeSe_2$ and GeSe (labeled as

CZGSe-A and CZGSe-B, respectively) are provided in Fig. 3 and S2.† The optimal temperature for CZGSe-A was 500 °C, and for CZGSe-B it was 600 °C. The different optimal temperatures may be due to the different Ge participating in the growth mechanism. CZGSe-A involves Ge first, followed by selenization. If the selenization temperature is too high, $GeSe_2$ easily evaporates again to cause the loss of Ge and the partial absorber layer to possibly decompose, similar to CZTSe.[31] A higher selenization temperature was tried but failed to obtain the pure CZGSe phase. Nevertheless, in the CZGSe-B sample, GeSe and Se vapors were involved together. If the temperature is low, the GeSe evaporates inadequately, which can easily cause a lack of Ge. In addition, GeSe vapor can also form liquid Ge_xSe_y with Se to promote the crystallization.[24] A more comprehensive and in-depth study of the formation process will be followed up in the future. Moreover, the elemental compositions of the CZGSe-A and CZGSe-B absorber layers are provided in Table S1.† The CZGSe-A and CZGSe-B samples below refer to the optimized ones used without special instructions. The SEM and EDX line mapping analyses showed that CZGSe-B had a better crystallinity and a uniform well-compact morphology. An interfacial $MoSe_2$ layer with a thickness of ~100 nm was observed in CZGSe-B. A thin $MoSe_2$ layer is well known to be able to convert Schottky into quasi-Ohmic contacts and facilitate carrier transport.[32,33] Thus, the CZGSe-B sample had a high-quality bulk absorber layer and good back interface, guaranteeing better device performance.

Fig. 3e shows the XRD patterns of the prepared CZGSe films. Three major peaks were observed in both samples and were assigned to the kesterite phase, indicating a single pure structure.[21,24] Noticeably, two other peaks were present in the CZGSe-B sample, belonging to $MoSe_2$, consistent with the observation of the morphological results. The Raman spectra for both were also recorded, as shown in Fig. 3f, with a 785 nm excitation wavelength, from which $MoSe_2$ could be detected. Apparently, the two peaks at 177 and 204.5 cm^{-1}, and one at 283 cm^{-1} were ascribed to the A and B modes of kesterite CZGSe, respectively.[21,34] The other prominent peak at 242 cm^{-1} could be unequivocally assigned to the A mode of $MoSe_2$,[35] confirming the previous results. Ge-based and other possible binary or ternary compounds were not detected.

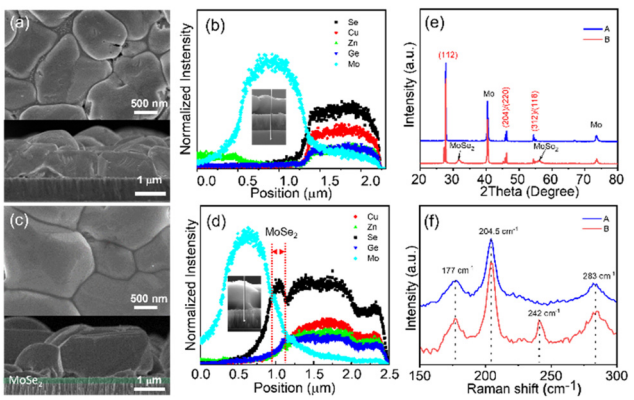

Fig. 3 (a–d) Surface and cross-sectional SEM images, and EDX line profiles of CZGSe absorbers (a and b: CZGSe-A; c and d: CZGSe-B). (e and f) XRD patterns and Raman spectra of CZGSe-A and CZGSe-B.

Grain boundaries (GBs), corresponding to the surface defects, highly affect the band structure and charge-separation characteristics.[36,37] KPFM was performed to ascertain the carrier-separation characteristics. Fig. 4 reveals the KPFM results of the surface potential (SP) and GB characteristics for the CZGSe-A and CZGSe-B absorber layers. In the SP images, the blue and yellow regions represent the high and low SP values, respectively. From the Z-position and SP plots in Fig. 4c and f, it could be observed that the GBs for CZGSe-A had higher potentials than the intragrains (IGs), whereas there were lower potentials for CZGSe-B. The SP differences between the GBs and IGs for the CZGSe-A and CZGSe-B absorber layers were statistically analyzed by counting the different regions in Fig. 4g. A positive value of 45 mV was obtained for the CZGSe-A absorber layer, indicating a higher SP was dominant at/near the GBs. Nevertheless, a negative value of −38 mV for the CZGSe-B absorber layer indicated a lower SP at/near the GBs, coinciding with the Z-position and SP plots.

A higher SP at/near the GBs means a downward band bending at the GBs, indicating that local built-in potential exists at the GBs, acting as an electron pathway and/or hole barrier.[38] Therefore, electrons are attracted to the GBs, and holes are repelled to the IGs in CZGSe-A. Yet, CZGSe-B brought about the opposite conclusions of upward band bending through the statistical analysis in Fig. 4g. The band bendings for CZGSe-A and CZGSe-B are illustrated in Fig. 4h. Previous studies have demonstrated that downward band bending at the GBs is favorable for the carrier separation and electron collection in CIGS- and CZTSSe-based absorber layers.[28,38,39] CZGSe is similar to CZTSe, with undesirable surface defect Cu_{Zn} predominating, mainly accumulated at/near the GBs. The downward bending band may cause the recombination of acceptor Cu_{Zn} defects and the collected electrons, at the expense of some photogenerated electrons at the GBs. Moreover, recent reports have illustrated that upward band bending ensures a higher device performance.[40,41] Therefore, the inversion of the band bending structure in CZGSe-B suggests it possessed a better surface junction to guarantee improved carrier separation.

A traditional configuration of SLG/Mo/CZGSe/CdS/i-ZnO/ITO/Ag grid solar cell device was fabricated, as presented in Fig. 5a. Apparently, the subsequent depositions of other functional layers (CdS, i-ZnO, and ITO) had no obvious impact on the CZGSe absorber layer. The statistic photovoltaic parameters for the CZGSe-A and CZGSe-B devices are given in Fig. 5b by accessing 20 individual cells. Due to the limitations of the electrodeposited process, each parameter showed large fluctuations. Nevertheless, the overall parameters for the CZGSe-B devices revealed a distinct increase, especially for V_{oc} and FF, indicating that the CZGSe-B devices possessed a better film quality and surface interface, along with good reproducibility. The *J–V* characteristics of the champion CZGSe-A and CZGSe-B solar cells are presented in Fig. 5c, and the corres-

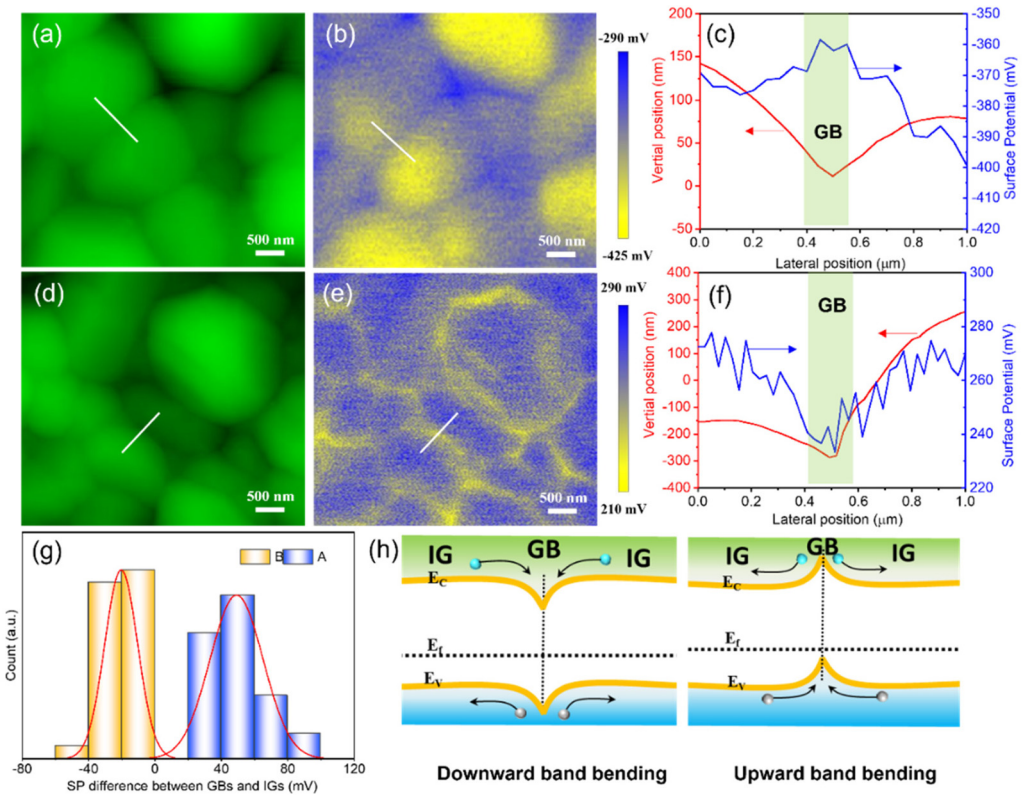

Fig. 4 (a and d) AFM surface topography, (b and e) KPFM SP images, (c and f) line profiles tracing the white lines for CZGSe-A and CZGSe-B absorber layers. (g) Statistic SP differences between GBs and IGs. (h) Schematic drawing of the energy band bendings near/at the GBs.

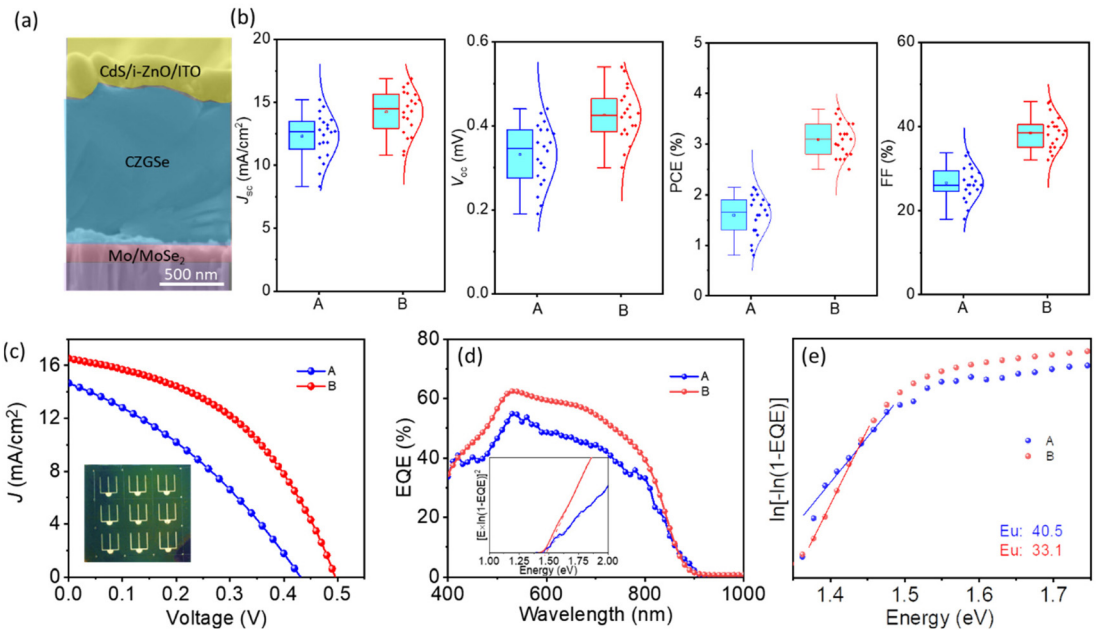

Fig. 5 (a) Cross-sectional image of the CZGSe-B based solar cell, (b) statistical performance parameters derived from 20 devices, (c) *J*–*V* curves, (d) EQE, and (e) Urbach energies (E_u) of the champion CZGSe solar cells. Insets of (c): optical image of the device, (d): band gaps extracted from the EQE.

Table 1 Main device parameters of the champion CZGSe cells

Devices	J_{sc} (mA cm^{-2})	V_{oc} (V)	FF (%)	E_{ff} (%)	R_s (Ω cm^2)	R_{sh} (Ω cm^2)	E_g/q–V_{oc} (eV)	E_g (eV)	E_u (meV)	A	J_0 (A cm^{-2})
CZGSe-A	14.66	0.43	33.78	2.14	1.2	490	1.02	1.45	40.5	2.64	6.7×10^{-6}
CZGSe-B	16.53	0.49	45.57	3.69	0.4	701	0.99	1.48	33.1	2.02	1.7×10^{-6}

ponding device parameters are summarized in Table 1. The CZTSe-A device presented a PCE of 2.14%, J_{sc} of 14.66 mA cm^{-2}, V_{oc} of 0.43 V, and FF of 33.78%. The CZGSe-B device exhibited a dramatically improved PCE of 3.69%, J_{sc} of 16.53 mA cm^{-2}, V_{oc} of 0.49 V, and FF of 45.57%. The CZGSe-B device showed a higher V_{oc} value, likely considered to be due to accelerated carrier transport due to the depressed surface defects and/or Fermi level pinning. The higher FF in the CZGSe-B device was due to the better carrier transport path through the inversion of the band bending. Moreover, it is important to note that CZGSe has not yet been prepared by an electrodeposition process. Diode parameters were extracted from the *J*–*V* curves, as shown in Fig. S3† and Table 1. The high V_{OC} deficit ($E_g/q - V_{OC}$), indicated large nonradiative recombination losses at the interface.[42] This suggest that deep-level/activated shallow-level defects at the CZTSSe/CdS interface still predominated, leading to a low efficiency. Besides, the large atomic fluctuation may have aggravated the compositional inhomogeneities and disorders, activating detrimental Cu_{Zn}–Ge_{Zn} deep-level defect clusters and increasing the antisite/shallow-level defects, thus leading to a deterioration in the device performance, as proved by the large A. Despite the low efficiency, we achieved the highest efficiency of the electrodeposited CZGSe and made an outstanding contribution to the development of green-processed CZGSe solar cells.

The EQE spectra in Fig. 5d show the improved photoelectric response in the overall response at 400–850 nm for the CZGSe-B device. These indicated a better carrier-collection capability benefiting from the enhanced bulk quality absorber and CZGSe/CdS interface. Besides, the bandgap energies for CZGSe-A and CZGSe-B were estimated to be 1.45 and 1.48 eV, as derived from the EQE curves in the inset of Fig. 5d, respectively. The E_g value of CZGSe-B was slightly higher than that of CZGSe-A, possibly owing to the suppression of defects/secondary phases within limits and the decrease in the nonstoichiometry of CZGSe-B.[43] Furthermore, the Urbach energies (E_u) were used to analyze the tail states, which are highly related to the fluctuations of the electrostatic potential caused by charged defects.[43] Here, E_u was obtained by fitting the reciprocal of the slope in the linear region, as presented in Fig. 5e. CZGSe-B showed a lower E_u value of 33.1 meV, indicating reduced cation disordering.[43,44]

C–*V* measurements of the CZGSe-A and CZGSe-B devices were performed to understand their internal limitations and to evaluate their p–n junction quality.[45] The corresponding carrier density ($N_{C\text{-}V}$) and depletion region width (W_d) could be derived from the *C*–*V* measurements, as depicted in Fig. 6a. The carrier density reflects the interface defect density contributed from the shallow/deep defects, while the depletion width represents the charge-separation ability. The carrier density of CZGSe-B was lower than that of CZGSe-A, indicating a reduced interface states density in CZGSe-B. Moreover, the depletion width of CZGSe-B (130 nm) was larger than that of CZGSe-A (120 nm), mainly ascribed to the reduced interface defects, indicating an improved p–n junction quality. Thus, the carrier separation could be enhanced, leading to a gradually improved FF. However, the interface states density in CZGSe was still high, possibly concurrently due to the complex shallow/deep defects at/near the interface and the lattice mismatch between CZGSe and CdS.[12] Besides, the CZGSe and CdS had "cliff-like" band alignments, further aggravating the interfacial recombination, causing a large V_{OC} loss.[16,18]

Admittance scans for CZGSe-A and CZGSe-B devices were also recorded, where the capacitance at high frequency related to the free carrier density, while that at low frequency referred to the sum of the deep traps and free carriers.[46,47] The frequency ranged from 10^3 to 10^7 Hz in the dark, along with a 30 mV AC voltage and DC bias at zero during the measurement. As shown in Fig. 6b, the capacitance of the CZGSe-B devices showed less frequency dependence than that of the CZTGSe-A devices, indicating the lower trap densities in the CZGSe-B devices, consistent with the *C*–*V* and DLTS results.

EIS was performed under AM 1.5 G solar illumination with 100 mW cm^{-2} light intensity to characterize the carrier transport/recombination behavior for the CZGSe-A and CZGSe-B devices in Fig. 6c. The intercept of the *x*-axis corresponds to the series resistance (R_s), related to the bulk/contact resistances. The diameter of the semicircle corresponds to the recombination resistance (R_p) at the interface between CZTSe and CdS.[43,48] The equivalent circuit in the inset was used to fit the R_s, R_p, and C values. The R_s values for the CZGSe-A and CZGSe-B devices were 30.2 and 13.7 Ω, respectively. The lower R_s for the CZGSe-B devices was mainly due to the better bulk quality and as $MoSe_2$ was involved in the back contact. The better surface junction formed an inversion of the band bending structure at the GBs and stimulated a visible increase in the R_p values in the CZGSe-B devices. The minority lifetimes (τ) for the CZGSe-A and CZGSe-B devices were quantified as 6.9 and 12.8 μs from the equation $\tau = R_p \times C$,[43] suggesting an improved carrier transport dynamic for the CZGSe-B devices. The improved carrier transport in the CZGSe-B device may be one of the main reasons for the V_{OC} and FF improvements.

C-DLTS was further conducted to evaluate the defects density for the CZGSe-A and CZGSe-B devices, as displayed in Fig. 6d and e. The measurements were tested in the temperature range from 120 to 240 K, which is the characteristic interval for Cu_{Zn} defects.[38] An apparent peak at ~180 K was observed in both samples, suggesting a defect energy level. The formation energies (E_a) and defect concentration (N_T)

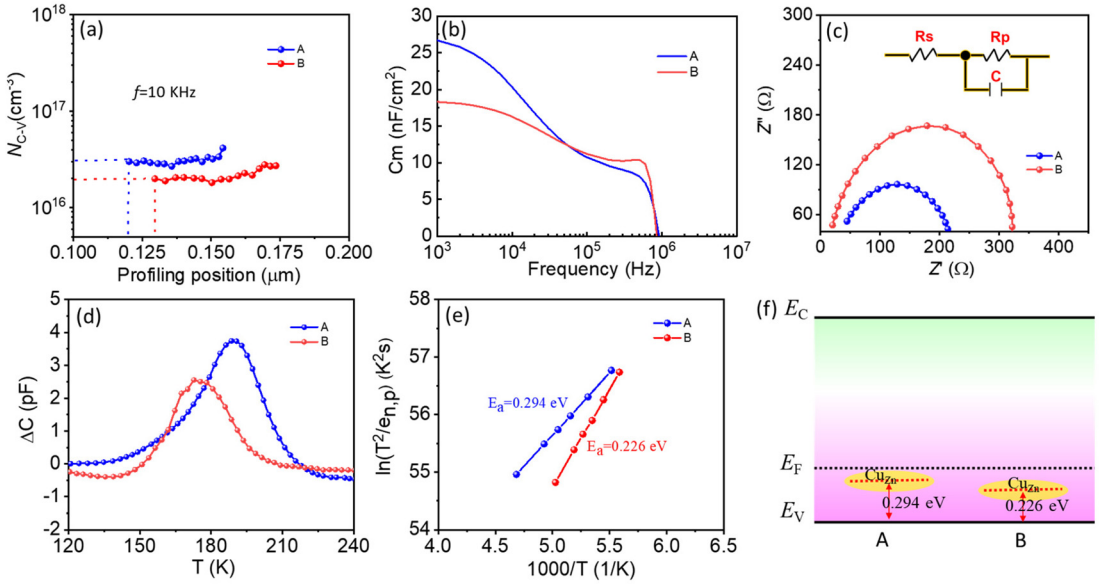

Fig. 6 (a) Calculated carrier density and W_d from the C–V measurements with 10 kHz frequency at room temperature, (b) frequency-dependent capacitance at room temperature, (c) EIS Nyquist plots and their corresponding equivalent circuit, (d and e) DLTS signals and Arrhenius plots, and (f) schematic diagram of the spatial distribution of Cu_{Zn} defects evaluated from DLTS measurements for CZGSe-A and CZGSe-B solar cells.

could be calculated from Arrhenius plots by the linear fitting of the points near the peaks. Here, E_a was 0.294 and 0.226 eV for the CZGSe-A and CZGSe-B devices, respectively, consistent with the value of Cu_{Zn} defects in CZGSe-based materials.[14] N_T was 2.83×10^{13} and 1.83×10^{13} cm^{-3} for the CZGSe-A and CZGSe-B devices, respectively. It is worth noting that the Cu_{Zn} defect was near the surface and close to E_F, which means it could easily cause Fermi level pinning and act as a recombination center, which is not conducive to the device performance. Thus, it can be inferred that the reduced Cu_{Zn} defect in the CZGSe-B devices would be reflected in the inversed electrical surface properties, mainly depressing interface recombination, leading to a better device performance.

4. Conclusions

In conclusion, we designed a synchronous strategy of Ge incorporation and selenization combined with an electrodeposition process to fabricate high-quality CZGSe thin films. A co-heating process of GeSe and Se was followed after electrodepositing a Cu–Zn preformed layer. Through a series of comparative characterization, it was found that the synchronous strategy offers a better bulk absorber layer and good back interface. This reversed the band bending, prolonged the depletion region width, and accelerated the charge separation and collection; consequently minimizing the recombination loss. With these numerous positive effects, the highest efficiency of 3.69% was achieved, representing the record for electrodeposited CZGSe solar cells. Our findings highly promote the development of green electrodeposited CZGSe solar cells.

Author contributions

Jingling Liu: conceptualization, methodology, data analysis, writing. Kang Gao: methodology, investigation, data analysis. Hang Cai and Xinyu Wu: investigation, data analysis. Xinsheng Liu: investigation, editing. Ke Cheng and Zuliang Du: supervision.

Conflicts of interest

There are no conflicts to declare.

Acknowledgements

This work was supported by the Programs for the National Natural Science Foundation of China (no. 61804045 and U1804160).

References

1 R. Aruna-Devi, M. Latha, S. Velumani and J. Á. Chávez-Carvayar, *Rare Met.*, 2021, **40**, 2602–2609.
2 B. Duan, L. Lou, F. Meng, J. Zhou, J. Wang, J. Shi, H. Wu, Y. Luo, D. Li and Q. Meng, *ACS Appl. Mater. Interfaces*, 2021, **13**, 55243–55253.
3 Q. Tian and S. Liu, *J. Mater. Chem. A*, 2020, **8**, 24920–24942.
4 National Renewable Energy Laboratory – Best Research-Cell Efficiency Chart, **https://www.nrel.gov/pv/cell-efficiency.html**.
5 N. Nisika, K. Kaur and M. Kumar, *J. Mater. Chem. A*, 2020, **8**, 21547–21584.

6 A. Fl, B. Sw, Z. C. Yi, D. Xh and E. Ld, *Sci. Bull.*, 2020, **65**, 698–701.
7 S. Chen, A. Walsh, X.-G. Gong and S.-H. Wei, *Adv. Mater.*, 2013, **25**, 1522–1539.
8 W. Chen, D. Dahliah, G.-M. Rignanese and G. Hautier, *Energy Environ. Sci.*, 2021, **14**, 3567–3578.
9 J. Li, D. Wang, X. Li, Y. Zeng and Y. Zhang, *Adv. Sci.*, 2018, **5**, 1700744.
10 K. Yin, X. Xu, M. Wang, J. Zhou, B. Duan, J. Shi, D. Li, H. Wu, Y. Luo and Q. Meng, *J. Mater. Chem. A*, 2022, **10**, 779–788.
11 M. Neuschitzer, M. E. Rodriguez, M. Guc, J. A. Marquez, S. Giraldo, I. Forbes, A. Perez-Rodriguez and E. Saucedo, *J. Mater. Chem. A*, 2018, **6**, 11759–11772.
12 S. Kim, J. A. Márquez, T. Unold and A. Walsh, *Energy Environ. Sci.*, 2020, **13**, 1481–1491.
13 S. Hadke, M. Huang, C. Chen, Y. F. Tay, S. Chen, J. Tang and L. Wong, *Chem. Rev.*, 2022, **122**, 10170–10265.
14 H. Nishihara, T. Maeda and T. Wada, *Jpn. J. Appl. Phys.*, 2018, **57**, 02CE06.
15 S. Sahayaraj, G. Brammertz, B. Vermang, T. Schnabel, E. Ahlswede, Z. Huang, S. Ranjbar, M. Meuris, J. Vleugels and J. Poortmans, *Sol. Energy Mater. Sol. Cells*, 2017, **171**, 136–141.
16 L. Choubrac, M. Bär, X. Kozina, R. Félix, R. G. Wilks, G. Brammertz, S. Levcenko, L. Arzel, N. Barreau, S. Harel, M. Meuris and B. Vermang, *ACS Appl. Energy Mater.*, 2020, **3**, 5830–5839.
17 R. Gunder, J. A. Márquez-Prieto, G. Gurieva, T. Unold and S. Schorr, *CrystEngComm*, 2018, **20**, 1491–1498.
18 K. Tsuji, T. Maeda and T. Wada, *Jpn. J. Appl. Phys.*, 2018, **57**, 08RC21.
19 T. Schnabel, M. Seboui and E. Ahlswede, *RSC Adv.*, 2017, **7**, 26–30.
20 D. B. Khadka and J. Kim, *CrystEngComm*, 2013, **15**, 10500–10509.
21 S. R. Rondiya, D. G. Buldu, G. Brammertz, Y. A. Jadhav, R. W. Cross, H. N. Ghosh, T. E. Davies, S. R. Jadkar, N. Y. Dzade and B. Vermang, *Phys. Chem. Chem. Phys.*, 2021, **23**, 9553–9560.
22 L. Choubrac, G. Brammertz, N. Barreau, L. Arzel, S. Harel, M. Meuris and B. Vermang, *Phys. Status Solidi A*, 2018, **215**, 1800043.
23 T. Schnabel, M. Seboui, A. Bauer, L. Choubrac, L. Arzel, S. Harel, N. Barreau and E. Ahlswede, *RSC Adv.*, 2017, **7**, 40105–40110.
24 N. Benhaddou, S. Aazou, R. Fonoll-Rubio, Y. Sánchez, S. Giraldo, M. Guc, L. Calvo-Barrio, V. Izquierdo-Roca, M. Abd-Lefdil, Z. Sekkat and E. Saucedo, *J. Mater. Chem. C*, 2020, **8**, 4003–4011.
25 J. Liu, S. Li, X. Liu, E. Jia, S. Chang, X. Shen, K. Cheng and Z. Du, *Sol. RRL*, 2019, **3**, 1900165.
26 J. Liu, Q. Shen, Z. Liu, X. Gao, Z. Zhang, X. Liu, K. Cheng and Z. Du, *ACS Appl. Mater. Interfaces*, 2021, **13**, 31852–31860.
27 K. Clauwaert, M. Goossens, J. De Wild, D. Colombara, P. J. Dale, K. Binnemans, E. Matthijs and J. Fransaer, *Electrochim. Acta*, 2016, **198**, 104–114.
28 Z. Zhang, Q. Gao, J. Guo, Y. Zhang, Y. Han, J. Ao, M.-J. Jeng, F. Liu, W. Liu and Y. Zhang, *Sol. RRL*, 2020, **4**, 2000059.
29 D. J. Xue, S. C. Liu, C. M. Dai, S. Chen, C. He, L. Zhao, J. S. Hu and L. J. Wan, *J. Am. Chem. Soc.*, 2017, **139**, 958–965.
30 J.-M. Wu, Y.-P. Lv, H. Wu, H.-S. Zhang, F. Wang, J. Zhang, J.-Z. Wang and X.-H. Xu, *Rare Met.*, 2022, **41**, 2992–2997.
31 J. J. Scragg, J. T. Wätjen, M. Edoff, T. Ericson, T. Kubart and C. Platzer-Björkman, *J. Am. Chem. Soc.*, 2012, **134**, 19330–19333.
32 S. Gao, Y. Zhang, J. Ao, S. Lin, Z. Zhang, X. Li, D. Wang, Z. Zhou, G. Sun, F. Liu and Y. Sun, *Sol. Energy Mater. Sol. Cells*, 2018, **176**, 302–309.
33 X. Zhu, Z. Zhou, Y. Wang, L. Zhang, A. Li and F. Huang, *Sol. Energy Mater. Sol. Cells*, 2012, **101**, 57–61.
34 E. Grau-Luque, I. Anefnaf, N. Benhaddou, R. Fonoll-Rubio, I. Becerril-Romero, S. Aazou, E. Saucedo, Z. Sekkat, A. Perez-Rodriguez, V. Izquierdo-Roca and M. Guc, *J. Mater. Chem. A*, 2021, **9**, 10466–10476.
35 N. Masurkar, N. K. Thangavel and L. M. R. Arava, *ACS Appl. Mater. Interfaces*, 2018, **10**, 27771–27779.
36 H. Xu, S. Ge, W. Yang, S. N. Khan, Y. Huang, Y. Mai, E. Gu, X. Lin and G. Yang, *J. Mater. Chem. A*, 2021, **9**, 25062–25072.
37 J. Zhou, X. Xu, B. Duan, H. Wu, J. Shi, Y. Luo, D. Li and Q. Meng, *Nano Energy*, 2021, **89**, 106405.
38 J. Fu, D. Kou, W. Zhou, Z. Zhou, S. Yuan, Y. Qi and S. Wu, *J. Mater. Chem. A*, 2020, **8**, 22292–22301.
39 K.-J. Yang, S. Kim, J.-H. Sim, D.-H. Son, D.-H. Kim, J. Kim, W. Jo, H. Yoo, J. Kim and J.-K. Kang, *Nano Energy*, 2018, **52**, 38–53.
40 K. Sardashti, R. Haight, T. Gokmen, W. Wang, L.-Y. Chang, D. B. Mitzi and A. C. Kummel, *Adv. Energy Mater.*, 2015, **5**, 1402180.
41 X. Zhao, X. Chang, D. Kou, W. Zhou, Z. Zhou, Q. Tian, S. Yuan, Y. Qi and S. Wu, *J. Energy Chem.*, 2020, **50**, 9–15.
42 S. K. Hwang, J. H. Park, K. B. Cheon, S. W. Seo, J. E. Song, I. J. Park, S. G. Ji, M. A. Park and J. Y. Kim, *Prog. Photovoltaics*, 2020, **28**, 1345–1354.
43 Y. Du, S. Wang, Q. Tian, Y. Zhao, X. Chang, H. Xiao, Y. Deng, S. Chen, S. Wu and S. Liu, *Adv. Funct. Mater.*, 2021, **31**, 2010325.
44 K. Nagaya, S. Fujimoto, H. Tampo, S. Kim, M. Nishiwaki, Y. Nishigaki, M. Kato, H. Shibata and H. Fujiwara, *Appl. Phys. Lett.*, 2018, **113**, 093901.
45 J. Fu, Q. Tian, Z. Zhou, D. Kou, Y. Meng, W. Zhou and S. Wu, *Chem. Mater.*, 2016, **28**, 5821–5828.
46 H.-S. Duan, W. Yang, B. Bob, C.-J. Hsu, B. Lei and Y. Yang, *Adv. Funct. Mater.*, 2013, **23**, 1466–1471.
47 X. Liu, C. Chen, L. Wang, J. Zhong, M. Luo, J. Chen, D.-J. Xue, D. Li, Y. Zhou and J. Tang, *Prog. Photovoltaics*, 2015, **23**, 1828–1836.
48 G. Wang, W. Zhao, Y. Cui, Q. Tian, S. Gao, L. Huang and D. Pan, *ACS Appl. Mater. Interfaces*, 2013, **5**, 10042–10047.